Size-controlled synthesis of spinel nickel ferrite nanorods by thermal decomposition of a bimetallic Fe/Ni-MOF

Bushra Iqbal^a, Andrea Laybourn^b, Anwar-ul-Hamid^c and Muhammad Zaheer^a*

^aDepartment of Chemistry and Chemical Engineering, Syed Babar Ali School of Science and Engineering, Lahore University of Management Sciences (LUMS), Lahore 54792 Pakistan

^bAdvanced Materials Research Group, Faculty of Engineering, University of Nottingham, Nottingham, NG7 2RD United Kingdom

^cCenter for Engineering Research, Research Institute, King Fahd University of Petroleum & Minerals, Dhahran 31261 Saudi Arabia

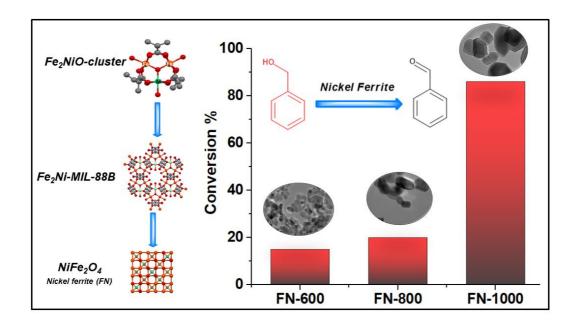
*Corresponding author: muhammad.zaheer@lums.edu.pk

Abstract

In this work, size-controlled synthesis of nickel ferrite nanoparticles was achieved by the calcination of a bimetallic (Fe/Ni) metal-organic framework (MOF). The bimetallic MOF (Fe₂Ni-MIL-88B) itself was prepared by a two-step route. The first step involved synthesis of the secondary building unit (SBU) by reacting stoichiometric amounts of Ni and Fe precursors with acetic acid. A ligand substitution reaction (terephthalate replaces acetate) in the SBU leads to the formation of the MOF, which was characterized by PXRD, FTIR, SEM and TEM. Afterwards, the MOF was calcined under air atmosphere to obtain nickel ferrite nanorods. PXRD analysis confirmed the spinel structure of the nickel ferrites while electron microscopic analysis (SEM, TEM) revealed their nanorod-like morphology. By increasing the calcination temperature from 600 to 1000°C, particle size increased from 16 to 32 nm. Oxidation of benzyl alcohol was used as a model test reaction to probe the applicability of spinel nickel

ferrite nanorods for catalysis. Interestingly, the largest nanorods exhibited the highest activity (86% conversion), thus demonstrating the potential of spinel ferrites in catalyzing oxidation reactions.

Graphical abstract



MOF derived nickel ferrites for benzyl alcohol oxidation

Keywords: Ferrites (D), calcination (A), functional applications (E), porosity (B)

1 Introduction

Spinel ferrites with general formula MFe₂O₄ (M = bivalent transition metals), have recently emerged as a class of technologically relevant magnetic materials possessing interesting properties.[1-3] Compared to their bulk counterparts, nanosized spinel ferrites show size dependent properties[4, 5] and offer great promise for a wide range of applications such as in magnetic and electronic devices,[6] gas sensing,[7] energy storage,[8] biomedicine, [9, 10] and catalysis.[11-14] These Fe-based complex oxides

are also renowned for their cost efficiency, non-toxicity, and natural abundance. Among spinel ferrites, nickel ferrite (NiFe₂O₄) is a well-known soft magnetic material having high chemical, thermal, and hydrothermal stability.[15, 16] It possesses an inverse spinel structure in which Ni2+ ions occupy octahedral corners, while Fe3+ ions are present both at octahedral and tetrahedral sites. Structural and catalytic properties of ferrites are greatly affected by their composition and method of preparation.[17] Various methods have been reported for synthesizing nanosized spinel ferrites, such as sol-gel, co-precipitation, solid-state, thermal decomposition, microwave heating, mechanochemical, solvothermal and hydrothermal routes.[18, 19] Solid-state methods are time consuming and require high temperatures, whereas co-precipitation requires stabilizing agents/surfactants and produces materials with a shorter shelf life and poor stability.[20] Although thermal decomposition methods can be used to prepare monosized nanoparticles (NPs), the use of high boiling solvents and surfactants results in coverage of the NP surface by capping agents which can lead to decreased catalytic activity.[21] Therefore, methods that provide high control over ferrite size and shape in the absence of capping agents are essential.

Metal-organic frameworks (MOFs) are the porous coordination polymers consisting of metal clusters and multidentate organic ligands joined via strong covalent bonding.[22] These porous materials with exceptionally high surface areas and tunable surface properties have been used for the development of porous metal oxide nanoarchitectures.[23] The heterometallic trinuclear oxo-clusters in mixed metal MOFs act as single-source precursors to synthesize different MOF-derived materials. This cluster synthesis route is an efficient way to control the composition and crystal phase by having the component elements mixed on the molecular level. This strategy also avoids the formation of other oxide side products.[24] The stoichiometry and

morphology of pristine MOF crystals can be transformed via calcination to corresponding metal oxide nanomaterials[25, 26] which exhibit uniform shape, hierarchical porosity[27], and high surface areas.[28-31] MOF-derived complex metal oxides and their nanocomposites show excellent potential for electromagnetic wave absorption,[32] volatile organic compound sensing,[33, 34] in catalysis[35, 36] and energy storage applications. [25, 37] For instance, MOF-derived NiFe₂O₄ nanorods, [33] AFe₂O₄ (A= Ni, Co, Zn) nanocubes,[38] NiFe₂O₄ polyhedra[34] and NiFe₂O₄ nanospheres[39] have been synthesized and used in toluene sensing, lithium ion storage, triethyl amine sensing and electrochemical water oxidation, respectively. In this work, we prepared a bimetallic MOF (Fe₂Ni-MIL-88B) via a cluster synthesis route[24], followed by its thermal decomposition in air to obtain nanocrystalline NiFe₂O₄ nanorods (NRs) of varying size. A stoichiometry of Fe:Ni (2:1) from the pristine MOF and to some extent, its porosity and crystal morphology was retained in the final spinel nickel ferrites. The spinel nickel ferrite NRs showed good activity in the oxidation of benzyl alcohol to benzaldehyde (up to 86 % conversion and 77-99 % selectivity). Our synthetic strategy, which negates the use of high boiling point solvents and surfactants, can potentially be extended to obtain other spinel ferrites such as CoFe₂O₄ and MnFe₂O₄.

2 Experimental

2.1 Materials and Methods

All the chemicals and reagents used in this work were of analytical grade. Nickel nitrate hexahydrate (Ni(NO₃)₂·6H₂O), iron nitrate nanohydrate (Fe(NO₃)₃·9H₂O), terephthalic acid (H₂BDC), sodium format, N,N-dimethylformamide (DMF) and ethanol solvents were purchased from Sigma-Aldrich and used as received.

2.2 Synthesis of Fe₂NiO-Cluster:

The Fe₂NiO-cluster which comprises the SBU in the subsequent MOF was synthesized using a procedure reported by Peng *et al.* [40] 7.3M aqueous solution of sodium acetate was prepared by adding 6 g of sodium acetate into 10 mL deionized water (solution A). Solution B was prepared by mixing Fe(NO₃)₃·9H₂O (1.14 g and Ni(NO₃)₂·6H₂O (4.15 g) in 10 mL DI-water. Combining solution, A and solution B resulted in a brown colored solution. After stirring for 24 hours, the brown powder was collected via centrifugation and washed with water (*ca.* 10 mL) and ethanol (*ca.* 10 mL). Finally, the product was dried in air. (Yield 6.77 g, 60 %).

2.3 Synthesis of Fe₂Ni-MIL-88B:

Fe₂Ni-MIL-88B was synthesized using the same procedure reported by Peng *et al.* with little modification in temperature and reaction time.[40] The Fe₂NiO-cluster (100 mg), terephthalic acid (100 mg), acetic acid (0.01M, 1 mL) and DMF (16 mL) were mixed in a glass vial. The mixture was ultrasonicated (for 15 minutes) and then heated in an oven at 110°C for 24 h. After cooling down to room temperature, the red-brown precipitate was collected by centrifugation, washed with DMF (5 mL x 3) and ethanol (5 mL x 3) and dried at 100°C under vacuum for 12 hours. (Yield 190 mg, 95 %).

2.4 Preparation of NiFe₂O₄ Nanorods:

Fe₂Ni-MIL-88B (150 mg) was calcined in a ceramic boat at 600°C (FN-600), 800°C (FN-800) and 1000°C (FN-1000) for 2 h in air using a ramp rate of 5°C min⁻¹.

2.5 General procedure for the oxidation of benzyl alcohol

To a round bottomed flask (50 mL) was added a mixture of benzyl alcohol (52 uL, 0.5 mmol), H₂O₂ (100 uL, 30 wt.% aqueous, 4.26 mmol), deionized water (3 mL) and

required amount of spinel nickel ferrite nanorods (see Table 2). The flask was then fitted with a condenser. The reaction mixture was stirred at 110°C for 4, 6, or 8 hours (see Table 2). After the completion of reaction, the spinel nickel ferrite catalyst was separated by centrifugation, and the remaining solution was subjected to GC-MS analysis after extraction with ethyl acetate (20 mL). Conversion and selectivity were calculated using GC-MS.

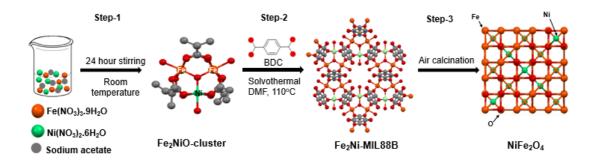
3 Results and Discussion

3.1 Overview of the Synthetic Route

Fabrication of nickel ferrite NRs consisted of three steps as presented in **Scheme 1**. In the first step, a bimetallic Fe₂NiO-cluster was synthesized *via* a previously reported procedure.[40] The metal ions in the cluster adopt a triangular arrangement with a μ₃-bridged oxygen at the center of the triangle. The terminal position of the octahedrally coordinated metal ions is occupied by water while each pair of metal ions is bridged with coordinated acetate ions.[41] The formation of the Fe₂NiO-cluster was confirmed by infrared (IR) spectroscopy and powder X-ray diffraction (PXRD) analysis (see **Figure 1 a** and **c**, respectively in Section 3.2).

In the second step, the bimetallic Fe₂NiO-cluster was reacted with terephthalic acid (H₂BDC) which replaced the acetate ligands leading to the formation of a bimetallic MOF, namely Fe₂Ni-MIL-88B. In the final step, Fe₂Ni-MIL-88B was calcined at

different temperatures (600, 800 and 1000 °C) which resulted in the formation of nickel ferrites NRs denoted FN-600, FN-800, and FN-1000.



Scheme 1 Schematic illustration of the synthetic route to NiFe₂O₄ nanorods.

3.2 Characterization of the Fe₂NiO-cluster and Fe₂Ni-MIL-88B MOF

The phase purity and crystallinity of both the cluster and MOF were analyzed by PXRD. The PXRD pattern of the Fe₂NiO-cluster synthesized in this work matches closely with that of the reported Fe₂NiO cluster (**Figure 1**a).[42] Likewise, the diffraction pattern of Fe₂Ni-MIL-88B is in agreement with the simulated MIL-88B pattern (**Figure 1**b). Here, high intensity reflection peaks (101), (002), (202) reveal the high crystallinity of the Fe₂Ni-MIL-88B MOF. Additionally, no extra peaks were detected, indicating the presence of a pure MIL-88B phase.[43] Formation of the MIL-88B structure was further confirmed by IR spectroscopy (**Figure 1c**).

IR spectra of both the Fe₂NiO-cluster and Fe₂Ni-MIL-88B MOF are presented in **Figure 1c**. In the IR spectrum of the Fe₂NiO-cluster strong absorption peaks are observed at 1579 and 1406 cm⁻¹ corresponding to coordinated -COO present in the acetate anions.[44-46] Further peaks in the range 400-800 cm⁻¹ corresponding to (M-O) vibrations in trinuclear cluster are also present, thus confirming the formation of Fe₂NiO-cluster.[47] Substitution of acetate by terephthalate and subsequent formation of Fe₂Ni-MIL-88B is confirmed by the presence of symmetric and antisymmetric vibrations of the BDC linker at 1373 cm⁻¹ and 1606 cm⁻¹, respectively.[45] M-O bonds

in Fe₂Ni-MIL88B have strong coordination compared to Fe₂NiO acetate cluster as indicated by the shift in antisymmetric vibrations from 1606 to 1579 cm⁻¹, respectively. Absence of a band at 1670 cm⁻¹ confirms the absence of free H₂BDC linker in the MOF while a peak at ~1650 cm⁻¹ indicated coordinated DMF in Fe₂Ni-MIL88B.[48]. The difference in the absorption peaks of Fe₂Ni-MIL-88B is smaller (v_{as^-} $v_s = 223$ cm⁻¹) than free H₂BDC linker (v_{as^-} $v_s = 391$ cm⁻¹) which is evidence of strong coordination between metals and bidentate ligand. Both spectra show a characteristic absorption peak associated with O-H stretching above 3400 cm⁻¹ ascribed to the presence of water in the metal coordination spheres. The presence of water in both the cluster and MOF is further confirmed by thermogravimetric analyses (**Figure 3a,b**).[46] Finally, the existence of μ_3 -oxo stretches (at 730 and 572 cm⁻¹ for acetate cluster, while 749 and

537 cm⁻¹ for Fe₂Ni-MIL-88B) indicates the presence of the same Fe₂NiO-cluster in both the cluster and the MOF.[49]

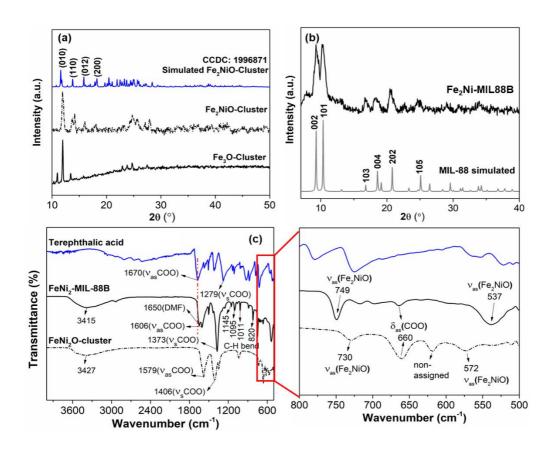


Figure 1 PXRD patterns of (a) Fe₂NiO-cluster and (b) Fe₂Ni-MIL-88B MOF, (c) FTIR spectra

The morphology, particle size and elemental composition of the Fe₂NiO-cluster and corresponding Fe₂Ni-MIL-88B MOF were investigated by Scanning Electron Microscopy (SEM), Transmission Electron Microscopy (TEM), and Energy Dispersive X-ray Spectroscopy (EDX). Fe₂NiO-clusters showed no regular morphology (**Fig. S1**). While Fe₂Ni-MIL-88B crystals appear as hexagonal nanorods (or spindles) of 674±116 nm in length and 81±6 nm in diameter (**Figure 2a-b**). EDX elemental mapping of the Fe₂NiO-cluster and Fe₂Ni-MIL-88B MOF revealed the homogenous distribution of Fe and Ni elements with a 2:1 mole ratio (**Fig. S2**). Fine details of the morphological aspects of Fe₂Ni-MIL-88B were obtained through TEM and representative micrographs are presented in **Figure 2c,d**. Hexagonal faces of the nanorods are clearly visible in

TEM micrographs which is in accordance with the spindle like morphology reported for MIL-88B.[50] The aspect ratio of Fe₂Ni-MIL-88B calculated from TEM images found to be 7 ± 3 nm.

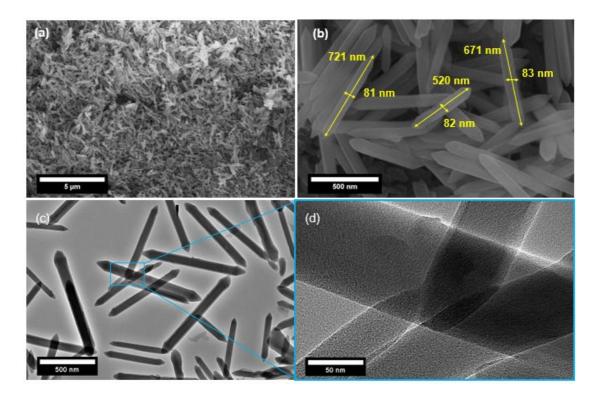


Figure 2 SEM images (a,b) and TEM images (c,d) of Fe₂Ni-MIL-88B at different magnifications (scale bars inset)

To assess thermal stability of the cluster compound and the MOF derived from it, thermogravimetric analysis (TGA) was performed in air. For the Fe₂NiO-cluster three different regions of mass losses were observed (**Figure 3a**). The first weight loss occurs at 100°C corresponding to the loss of the surface adsorbed H₂O molecules while a 9% weight loss at 170°C is attributed to the loss of coordinated H₂O. Decomposition of the Fe₂NiO-cluster starts at 240 °C and is complete at around 390 °C. A total weight loss of almost 50% at this step agrees with the empirical formula [Fe₂NiO(CH₃CO₂)₆(H₂O)₃] of the trinuclear acetate cluster.[51]

In case of Fe₂Ni-MIL-88B, the first weight loss occurs before 100°C owing to the loss of surface absorbed water and DMF from the pores/channels of the MOF. The second

step involving removal of coordinated DMF occurs between 100 and 200°C corresponding to an empirical formula of [Fe₂NiO(BDC)₃(DMF)₃.DMF]. Weight loss above 220°C is assigned to decomposition of organic linker. Unreacted BDC linker sublime prior to decomposition temperature (276-382°C). There is no rapid weight loss around this temperature which is the indirect evidence for the absence of unreacted linker.[52] The Fe₂Ni-MIL-88B structure fully decomposes above 600°C suggesting the higher stability of the bimetallic MOF compared to the reported monometallic MIL-88A, MIL-88C and MIL-88D but consistent with MIL-88B structures.[53, 54] We accredit improved stability to the addition of divalent Ni²⁺ ions in the cluster which form strong coordination with terminal ligand (DMF) due to the fact that crystal field stabilization energy of Ni²⁺ is higher as compared to trivalent Fe³⁺ (**Figure 3b**).[49]

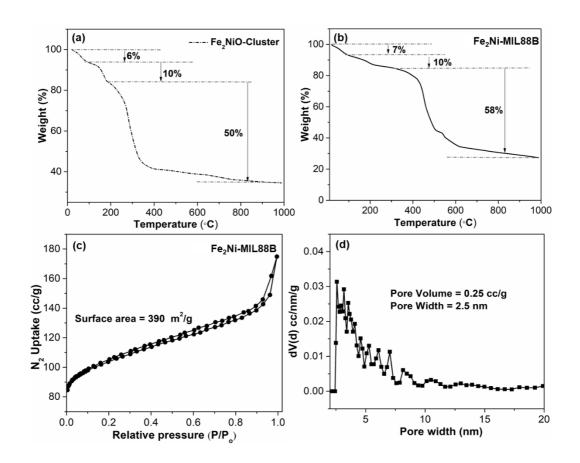


Figure 3 TGA of (a) Fe₂NiO-Cluster and (b) Fe₂Ni-MIL-88B. (c) N₂ adsorption-desorption isotherm and (d) pore size distribution of Fe₂Ni-MIL-88B measured at 77 K. Pore size distributions calculated from the adsorption branch of the isotherm, using NLDFT model

 N_2 -physisorption at 77 K was used to measure the surface area and pore size of Fe_2Ni -MIL-88B. Surprisingly, Fe_2Ni -MIL-88B showed a surface area of 390 m²/g even though MIL-88B(Fe) structures (containing Fe_3O clusters) are known to have low surface areas of ~160 m²/g due to the presence of compensating anions inside the pores.[55] Vuong and coworkers suggested that MIL-88B MOFs containing bimetallic Fe_2NiO -clusters avoid these compensating anions, which is why they possess a higher surface area than the equivalent monometallic MOFs.[48] The Type-II adsorption-desorption isotherm of Fe_2Ni -MIL-88B indicates the presence of mesopores in the structure.[56] The point of inflection at a relative pressure ($P/P_0 < 0.2$) is ascribed to the formation of a gas monolayer, while between P/P_0 0.2 and 0.9 multilayer adsorption

occurs (**Figure 3c**).[30] Fe₂Ni-MIL-88B exhibits a broad pore size distribution (2-10 nm) as modelled using Non-Local Density Functional Theory (NLDFT) method (**Figure 3**d). Majority of the N₂ adsorption occurs at low relative pressure (P/P_o<0.2), hence indicative of mesoporosity in material. The average pore size of Fe₂Ni-MIL-88B is 2.5 nm calculated using the equilibrium model of NLDFT (spherical pores) for mesoporous materials and is consistent with the reported MIL-88 structures.

3.3 Characterization of air calcined Fe₂Ni-MIL-88B

PXRD patterns of Fe₂Ni-MIL-88B calcined at different temperatures are shown in (**Figure 4a**). These patterns display typical peaks of a polycrystalline material. The relative intensities at specific 2θ (°) values are in good agreement with the face centered cubic (FCC) spinel-type nickel ferrite structure (JCPDS No. 10-0325). Average crystallite sizes of the spinel nickel ferrites NRs, calculated by Scherrer formula from the most intense peak ($2\theta = 35^{\circ}$), are 17 ± 2 nm, 25 ± 1 nm and 32 ± 1 nm for FN-600, FN-800 and FN-1000, respectively. Crystallite size was found to increase with temperature (due to Ostwald ripening) thus resulting in narrowing of the diffraction peaks.[57] This shows that the size of the spinel nickel ferrite NRs can be controlled by altering the calcination temperature.

IR spectra, in 4000–350 cm⁻¹ range for NiFe₂O₄ formed at various temperatures are shown in (**Figure 4b**). The broad peak near 3383 cm⁻¹ could be attributed to the O-H stretching vibration present on the surface of nickel ferrites as well as absorbed H₂O molecules. The specific bands for metal-oxygen stretching from the tetrahedral site appears in 584–540 cm⁻¹ range and from the octahedral site below 400 cm⁻¹.[58] These

results quite match with the XRD and SEM results which confirm that the ferrite particles have spinal structure.

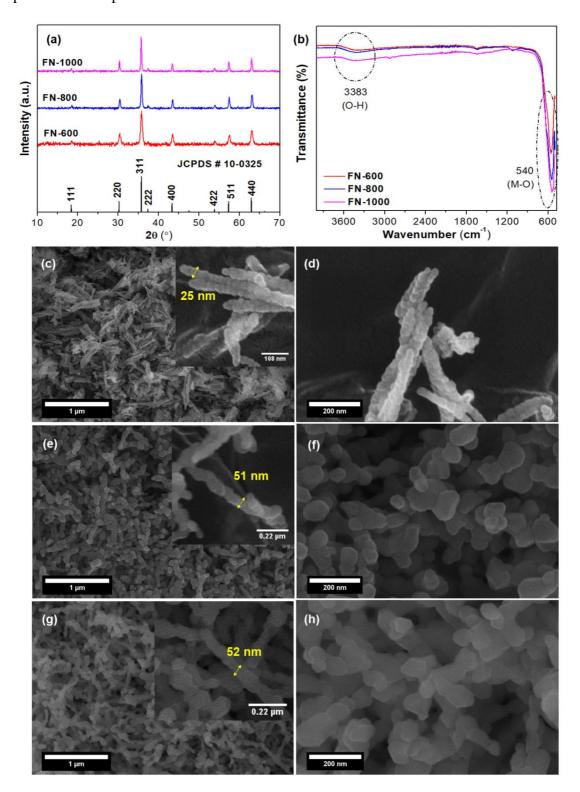


Figure 4 (a) PXRD patterns and (b) FTIR spectra of the nickel ferrites. SEM images of (c,d) FN-600, (e,f) FN-800, (g,h) FN-1000 at varying magnification. Scale bars inset

The morphology and composition of the spinel nickel ferrites were investigated using a combination of SEM, TEM and EDX. SEM images presented in **Figure 4c-h** show that the spinel nickel ferrites maintain the elongated structure of MIL-88, though they are more like nanorods instead of hexagonal spindles. Images taken at higher magnification show that all spinel nickel ferrites are morphologically similar and that the nanorods appear to be comprised of self-assembled NPs. This is further evident in the TEM images discussed later (**Figure 5**). The average diameters of FN-1000, FN-800 and FN-600 nanorods were calculated to be 52 ± 12 nm, 51 ± 8 nm and 25 ± 3 nm, respectively indicating an increase in nanorod size with increasing temperature in agreement with PXRD analyses. The width of the nanorods was found to be smaller than that of the MOF crystals from which they were formed (width: 81 ± 6 nm). We ascribe the reduction in length of the nanorods to evolution of gases arising from decomposition of the organic ligands during the calcination of Fe₂Ni-MIL-88B. EDX elemental mapping of the spinel nickel ferrites shows that Fe, Ni and O are uniformly distributed (**Fig. S3a-c**). The mole % of Fe/Ni ratio in the Fe₂NiO-cluster, Fe₂Ni-MIL-

88B and all three nickel ferrite samples calculated from EDX is consistent with theoretical calculation (**Fig. S3d**).

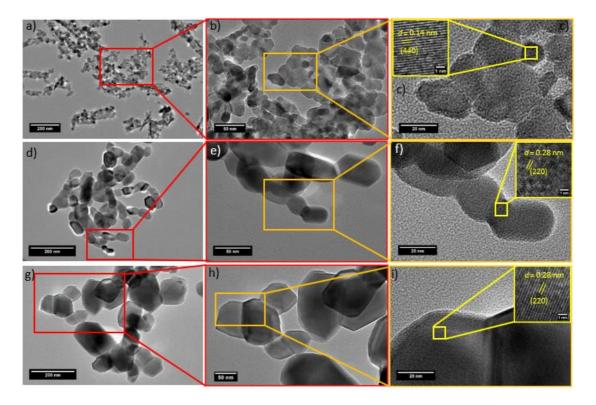


Figure 5 TEM images and corresponding HR-TEM image (fringes) of (a-c) FN-600, (d-f) FN-800, (g-i) FN-1000

As mentioned earlier in this section, TEM micrographs show the spinel nickel ferrite nanorods are comprised of irregularly shaped (FN-600), hexagonal (FN-800) or polyhedral (FN-1000) nanoparticles (NPs) with distinct grain boundaries (**Figure 5**). The size of these NPs increases drastically with increasing calcination temperature from 17±3 nm at 600 °C to 47±8 nm at 800°C whereas only a slight increase in size (53±13 nm) is observed at 1000°C. Particle sizes determined from TEM images are in accordance with SEM and PXRD results. It has been reported earlier that calcination process generally cause coalescence of smaller grains that results in increasing the average grain size.[59] The high resolution TEM (HR-TEM) images indicate that the nickel ferrite NPs (within the NRs) are crystalline with hexagonal or polyhedral shapes with distinct fringes (**Fig. 5a-i**). A d-spacing of 0.28 nm in the HR-TEM images of FN-

800 and FN-1000 (measured using ImageJ software) correspond to the (220) plane of fcc nickel ferrite. An interplanar spacing of 0.14 nm, in case of FN-600 was indexed to the (440) plane.[60]

A summary of the surface areas and pore size distributions of Fe₂Ni-MIL-88B and the nickel ferrites are listed in **Table 1**. The surface area, pore diameter and pore volume of the nickel ferrites were greatly affected by calcination temperature. Transition of Fe₂Ni-MIL-88B to nickel ferrites is associated with a huge reduction in the surface area (from 390 to 48 m²/g) due to the collapse of 3D MOF-network. Within nickel ferrites, the surface area increased with calcination temperature from 48 to 66 and then 95 m²/g for FN-600, FN-800, and FN-1000, respectively. Pore diameter, on the other hand, decreased in the same order. This can be attributed to the densification of the materials upon increasing temperature. Escape of gases during the decomposition of the organic linker lead to high surface area.[61] TGA of bimetallic MOF shows small mass loss after 600°C and 800°C, corresponding to the removal of some residual gaseous species which might be the reason why the surface area increased with increasing temperature (**Figure S4**). The N₂ adsorption/desorption isotherms of the nickel ferrites are shown in Figure 6. FN-600 exhibits a Type-IV isotherm with hysteresis loops indicating the presence of mesopores. FN-800 and FN-1000 display Type-II isotherms indicative of N₂ adsorption taking place on external surfaces.[56] The presence of hysteresis loops in all isotherms, is a result of capillary condensation.[62]

Table 1 Summary of porous properties of Fe₂Ni-MIL-88B and the MOF-derived nickel ferrites

Material	BET Surface area (m ² /g) ^{a,b}	Total Pore volume (cc/g) ^{c,d}	Pore width (nm)
Fe ₂ Ni-MIL-88B	390	0.25	2.5
FN-600	48	0.17	6.0

FN-800	66	0.11	4.9	
FN-1000	95	0.14	4.1	

 $[^]a$ Values given to zero decimal places, b P/P $_0$ range 0.01 to 0.04, c Total pore volume at P/P $_0$ = 0.99, d

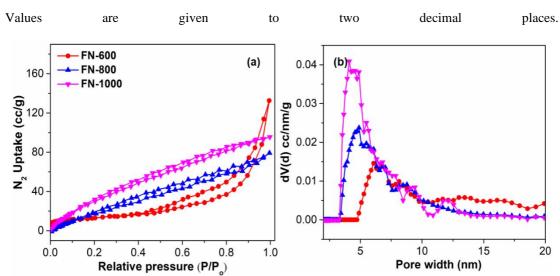


Figure 6 (a) N₂ adsorption-desorption isotherm and (b) pore size distribution of nickel ferrites measured at 77 K. Pore size distributions calculated from the adsorption branch of the isotherm, using NLDFT model for mesoporous materials. Legend inset

4 Catalytic oxidation of benzyl alcohol

The catalytic activity of the as-prepared nickel ferrites were tested using the oxidation of benzyl alcohol as a model test reaction. [63] Benzyl alcohol oxidation is one of the most important reactions in chemical industry because of high demand of benzaldehyde as an intermediate for the production of many chemicals, flavoring agents, textile dyes, and fragrances. [64] Moreover, benzyl alcohol moiety is a part of the β -O-4 ether bonds contained by the lignin [65]. Oxidation of this benzylic alcohol is important in the catalytic depolymerization of lignin to obtain aromatic compounds. [66] In this work, the reaction was carried out at 110 °C in deionized-water using hydrogen peroxide (H₂O₂) as an oxidizing agent under base-free conditions. H₂O₂ was chosen as it is cheaper and non-toxic compared to other oxidants, additionally its decomposition

products are solely oxygen and water. Moreover, H_2O_2 is reported to promote exchange of oxidation states between Fe^{3+} and Ni^{2+} and so the combination of H_2O_2 as an oxidant and nickel ferrites as a catalyst is a suitable for oxidation reactions.[67]

During the oxidation reaction, in addition to benzaldehyde and benzoic acid, side-products may also form. Potential side-products include toluene, benzyl benzoate, benzoic acid and dibenzyl ether as the result of dehydration or following a disproportionation reaction.[63] Reactions performed herein produced exclusively benzaldehyde and benzoic acid (**Scheme 2**).

Scheme 2 Nickel ferrite catalyzed oxidation of benzyl alcohol in H₂O₂

Initially, a blank experiment (without catalyst) was run which showed negligible activity (entry 1,

Table 2). Further control experiments were performed using the monometallic MIL-88B(Fe)and bimetallic Fe2Ni-MIL-88B MOFs which gave 10 % and 12% conversion to benzaldehyde, respectively (entries 2-3,

Table 2). Encouragingly, the nickel ferrites exhibited good activity for benzyl alcohol oxidation which partly, could be due the presence of mesopores which favor effective mass transport. First, FN-600 was examined as a catalyst which gave 15 % conversion of benzyl alcohol to benzaldehyde in 6 hours without any side products. Although the conversion is low, the selectivity toward benzaldehyde formation was

high (99%). The conversion of benzyl alcohol increased from 15 % to 24 % when FN-800 was used as the catalyst (entry 4 c.f. entry 5,

Table 2). However, among all of the nickel ferrites FN-1000 (*i.e.*, the material prepared at 1000°C and exhibiting the highest surface area) was the most active (entry 6,

Table 2) and was selected for further studies involving varying reaction time and catalyst amount (entries 7-10,

Table 2 Optimization of reaction conditions for the oxidation of benzyl alcohol to benzaldehyde

Table 2).

Entry	Catalyst	Time	Catalyst dosage	Conversion	Selectivity (%)	
		(hour)	(mmol)	(%)	Benzaldehyde	Benzoic
						acid
1	Blank	6	0	9	-	-
2	Fe-MOF	6	0.08	10	-	-
3	Fe/Ni-MOF	6	0.08	12	-	-
4	FN-600	6	0.08	15	99	-
5	FN-800	6	0.08	20	99	-
6	FN-1000	6	0.08	86	77	22
7	FN-1000	6	0.04	7	99	
8	FN-1000	6	0.1	42	99	-
9	FN-1000	4	0.08	20	99	-
10	FN-1000	8	0.08	70	99	-

Reaction conditions: benzyl alcohol (50 uL, 0.5 mmol), DI-water (3 mL), H_2O_2 (100 uL, 30 wt.%, 4.26 mmol) as oxidant, temperature (110°C) and catalyst amount (x mg, x = 10, 20,25)

The effect of catalyst loading was studied using three different quantities of FN-1000, i.e. 0.04, 0.08 and 0.1 mmol; entries 7, 8, and 9-10, respectively (

Table 2) whilst keeping the other parameters constant. An increase in catalyst amount from 0.04 to 0.08 mmol led to an increase in conversion from 7 % to 86 %, as anticipated. However, with 0.1 mmol, the conversion fell to 42%. This decrease in conversion at high catalyst amount may be a consequence of deactivation of the catalyst surface by absorption of oxidized products.

The effect of time was investigated by performing reactions for 4 and 8 hours (entries 9 and 10, respectively,

Table 2). Changing the reaction time from 6 to 4 hours (entry 6 c.f. 9,

Table 2) and from 6 to 8 hours (entry 6 *c.f.* 10,

Table 2) both resulted in a decrease in conversion. We tentatively ascribe the decrease in conversion and selectivity at 8 hours to deactivation of the catalyst at prolonged reaction times.

After screening reaction time, and catalyst type and amount, the optimal reaction conditions for conversion of benzyl alcohol to benzaldehyde in deionized water at 110 °C using H₂O₂ as an oxidizing agent were: 0.08 mmol FN-1000 catalyst, for 6 hours. Under these conditions, the conversion of benzyl alcohol over FN-1000 was 86 % and the selectivity to benzaldehyde was 77 %. The conversion achieved here is higher than many reported catalysts which typically use environmentally unfriendly bases and solvents (Table S1). Along with benzaldehyde, 22 % benzoic acid was formed during the reaction as a side product due to over oxidation. So, it can be concluded that ferrites prepared at lower temperature (FN-600 and FN-800, prepared at 600 and 800 °C respectively) showed greater selectivity towards the less oxidized benzaldehyde product, while nickel ferrite produced at 1000 °C (FN-1000) exhibited greater selectivity towards the more oxidized product, i.e. benzoic acid.

5 Conclusions

Metal organic frameworks (MOFs) have emerged as a versatile candidate for the preparation of various nanostructures with controllable size and composition. Herein a series of spinel NiFe₂O₄ with varying size and structure were prepared from the calcination of a bimetallic Fe₂Ni-MIL-88B MOF. The MOF itself was synthesized by reacting terephthalic acid with a bimetallic acetate cluster. Finally, hexagonal rods of Fe₂Ni-MIL-88B were transformed into NiFe₂O₄ nanorods via air calcination at varying temperatures. These nanorods consisting of tiny crystalline nanoparticles joined end to end in a chain and showed good activity towards the oxidation of benzyl alcohol under mild conditions. The surface area and size of NiFe₂O₄ nanoparticles greatly affect the activity of catalyst. Ferrite possessing high specific surface area offered high conversion (86%) along with high selectivity (77%) for benzaldehyde. The high surface area and porous structure is believed to be responsible for high catalytic activity towards oxidation reaction. This work provides a rational approach to synthesize various MOF derived ferrites for other catalytic applications for future.

Acknowledgements

M.Z. acknowledges the financial support from Higher Education Commission (HEC) of Pakistan under National Research Program for Universities (NRPU grant #4130 and 5910). B.I. is grateful to HEC for sponsoring a short-term stay in University of Nottingham under IRSIP program.

Declaration of competing interest

The authors declare that they have no known competing financial interests or personal relationships that could have appeared to influence the work reported in this paper.

CRediT Author Statement

Bushra Iqbal: Investigation, writing-Original Draft **Andrea Laybourn:**Conceptualization, Writing-Review & Editing **Anwar ul-Hamid:** Resources, visualization **Muhammad Zaheer:** Conceptualization, Supervision, Project administration, Funding acquisition, Writing-Review & Editing

References

- [1] S.B. Narang, K. Pubby, Nickel Spinel Ferrites: A Review, Journal of Magnetism and Magnetic Materials, (2020) 167163.
- [2] R.C. Pullar, Hexagonal ferrites: a review of the synthesis, properties and applications of hexaferrite ceramics, Progress in Materials Science, 57 (2012) 1191-1334.
- [3] L. Jaswal, B. Singh, Ferrite materials: A chronological review, Journal of Integrated Science and Technology, 2 (2014) 69-71.
- [4] B. Paul, D.D. Purkayastha, S.S. Dhar, Size-controlled synthesis of NiFe2O4 nanospheres via a PEG assisted hydrothermal route and their catalytic properties in oxidation of alcohols by periodic acid, Applied Surface Science, 370 (2016) 469-475.
- [5] C. Liu, Z.J. Zhang, Size-Dependent Superparamagnetic Properties of Mn Spinel Ferrite Nanoparticles Synthesized from Reverse Micelles, Chemistry of Materials, 13 (2001) 2092-2096.
- [6] W. Zhu, L. Wang, R. Zhao, J. Ren, G. Lu, Y. Wang, Electromagnetic and microwave-absorbing properties of magnetic nickel ferrite nanocrystals, Nanoscale, 3 (2011) 2862-2864.
- [7] A. Šutka, K.A. Gross, Spinel ferrite oxide semiconductor gas sensors, Sensors and Actuators B: Chemical, 222 (2016) 95-105.
- [8] M. Fu, Z. Zhu, Y. Zhou, W. Xu, W. Chen, Q. Liu, X. Zhu, Multifunctional pompon flower-like nickel ferrites as novel pseudocapacitive electrode materials and advanced absorbing materials, Ceramics International, 46 (2020) 850-856.
- [9] X. Lasheras, M. Insausti, I. Gil de Muro, E. Garaio, F. Plazaola, M. Moros, L. De Matteis, J.s. M. de la Fuente, L. Lezama, Chemical synthesis and magnetic properties of monodisperse nickel ferrite nanoparticles for biomedical applications, The Journal of Physical Chemistry C, 120 (2016) 3492-3500.
- [10] K.K. Kefeni, T.A.M. Msagati, T.T.I. Nkambule, B.B. Mamba, Spinel ferrite nanoparticles and nanocomposites for biomedical applications and their toxicity, Materials Science and Engineering: C, 107 (2020) 110314.
- [11] H. Zheng, Y. Ni, N. Xiang, X. Ma, F. Wan, Solvothermal synthesis of octahedral NiFe 2 O 4 nanocrystals and catalytic properties for the reduction of some aromatic nitrocompounds, Materials Chemistry and Physics, 158 (2015) 82-88.
- [12] D. Hong, Y. Yamada, T. Nagatomi, Y. Takai, S. Fukuzumi, Catalysis of nickel ferrite for photocatalytic water oxidation using [Ru(bpy)3]2+ and S2O8(2-), Journal of the American Chemical Society, 134 (2012) 19572-19575.
- [13] D. Hong, Y. Yamada, M. Sheehan, S. Shikano, C.-H. Kuo, M. Tian, C.-K. Tsung, S. Fukuzumi, Mesoporous Nickel Ferrites with Spinel Structure Prepared by an Aerosol Spray Pyrolysis Method for Photocatalytic Hydrogen Evolution, ACS Sustainable Chemistry & Engineering, 2 (2014) 2588-2594.
- [14] B.I. Kharisov, H.V.R. Dias, O.V. Kharissova, Mini-review: ferrite nanoparticles in the catalysis, Arabian Journal of Chemistry, 12 (2019) 1234-1246.

- [15] C.J. O'Brien, Z. Rák, D.W. Brenner, Calculated Stability and Structure of Nickel Ferrite Crystal Surfaces in Hydrothermal Environments, The Journal of Physical Chemistry C, 118 (2014) 5414-5423.
- [16] J. Zhang, R. Shu, C. Guo, R. Sun, Y. Chen, J. Yuan, Fabrication of nickel ferrite microspheres decorated multi-walled carbon nanotubes hybrid composites with enhanced electromagnetic wave absorption properties, J. Alloys Compd., 784 (2019) 422-430.
- [17] R. Benrabaa, H. Boukhlouf, E. Bordes-Richard, R.N. Vannier, A. Barama, Nanosized nickel ferrite catalysts for CO2 reforming of methane at low temperature: effect of preparation method and acid-base properties, in: Studies in Surface Science and Catalysis, Elsevier, 2010, pp. 301-304.
- [18] A. Hajalilou, S.A. Mazlan, A review on preparation techniques for synthesis of nanocrystalline soft magnetic ferrites and investigation on the effects of microstructure features on magnetic properties, Applied Physics A, 122 (2016) 680.
- [19] R. Shu, J. Zhang, C. Guo, Y. Wu, Z. Wan, J. Shi, Y. Liu, M. Zheng, Facile synthesis of nitrogen-doped reduced graphene oxide/nickel-zinc ferrite composites as high-performance microwave absorbers in the X-band, Chem. Eng. J., 384 (2020) 123266. [20] M. Kumari, M.C. Bhatnagar, Optimization of the behavior of CTAB coated cobalt ferrite nanoparticles, in: AIP Conference Proceedings, AIP Publishing LLC, 2018, pp. 030265.
- [21] A. Quintanilla, V.C.L. Butselaar-Orthlieb, C. Kwakernaak, W.G. Sloof, M.T. Kreutzer, F. Kapteijn, Weakly bound capping agents on gold nanoparticles in catalysis: Surface poison?, Journal of Catalysis, 271 (2010) 104-114.
- [22] H. Furukawa, K.E. Cordova, M. O'Keeffe, O.M. Yaghi, The chemistry and applications of metal-organic frameworks, Science, 341 (2013).
- [23] Y.V. Kaneti, J. Tang, R.R. Salunkhe, X. Jiang, A. Yu, K.C. Wu, Y. Yamauchi, Nanoarchitectured Design of Porous Materials and Nanocomposites from Metal-Organic Frameworks, Advanced materials, 29 (2017).
- [24] M. Bosch, S. Yuan, W. Rutledge, H.-C. Zhou, Stepwise synthesis of metal–organic frameworks, Accounts of Chemical Research, 50 (2017) 857-865.
- [25] Y. Li, Y. Xu, W. Yang, W. Shen, H. Xue, H. Pang, MOF-derived metal oxide composites for advanced electrochemical energy storage, Small, 14 (2018) 1704435.
- [26] R. Shu, Y. Wu, W. Li, J. Zhang, Y. Liu, J. Shi, M. Zheng, Fabrication of ferroferric oxide-carbon/reduced graphene oxide nanocomposites derived from Fe-based metal-organic frameworks for microwave absorption, Compos. Sci. Technol., (2020) 108240.
- [27] N. Abdollahi, A. Morsali, Catalytic improvement by open metal sites in a new mixed-ligand hetero topic metal-organic framework, Polyhedron, (2018).
- [28] S. Dang, Q.-L. Zhu, Q. Xu, Nanomaterials derived from metal–organic frameworks, Nature Reviews Materials, 3 (2017) 1-14.
- [29] K.Y. Zou, Z.X. Li, Controllable Syntheses of MOF-Derived Materials, Chemistry–A European Journal, 24 (2018) 6506-6518.
- [30] J. Wang, J. Wan, Y. Ma, Y. Wang, M. Pu, Z. Guan, Metal-organic frameworks MIL-88A with suitable synthesis conditions and optimal dosage for effective catalytic degradation of Orange G through persulfate activation, RSC advances, 6 (2016) 112502-112511.
- [31] G. Férey, C. Mellot-Draznieks, C. Serre, F. Millange, J. Dutour, S. Surblé, I. Margiolaki, A chromium terephthalate-based solid with unusually large pore volumes and surface area, Science, 309 (2005) 2040-2042.
- [32] R. Shu, W. Li, Y. Wu, J. Zhang, G. Zhang, Nitrogen-doped Co-C/MWCNTs nanocomposites derived from bimetallic metal–organic frameworks for electromagnetic wave absorption in the X-band, Chem. Eng. J., 362 (2019) 513-524.
- [33] Y. Zhang, C. Jia, Q. Wang, Q. Kong, G. Chen, H. Guan, C. Dong, Highly Sensitive and Selective Toluene Sensor of Bimetallic Ni/Fe-MOFs Derived Porous NiFe2O4 Nanorods, Industrial & Engineering Chemistry Research, 58 (2019) 9450-9457.

- [34] C. Zhai, H. Zhang, L. Du, D. Wang, D. Xing, M. Zhang, Nickel/iron-based bimetallic MOF-derived nickel ferrite materials for triethylamine sensing, CrystEngComm, 22 (2020) 1286-1293.
- [35] N. Martín, M. Dusselier, D.E. De Vos, F.G. Cirujano, Metal-Organic framework derived metal oxide clusters in porous aluminosilicates: A catalyst design for the synthesis of bioactive aza-heterocycles, ACS Catalysis, 9 (2018) 44-48.
- [36] X. Wang, J. Ying, Y. Mai, J. Zhang, J. Chen, M. Wen, L. Yu, MOF-derived metal oxide composite Mn 2 Co 1 O x/CN for efficient formaldehyde oxidation at low temperature, Catalysis Science & Technology, 9 (2019) 5845-5854.
- [37] R.R. Salunkhe, Y.V. Kaneti, Y. Yamauchi, Metal-organic framework-derived nanoporous metal oxides toward supercapacitor applications: progress and prospects, ACS nano, 11 (2017) 5293-5308.
- [38] J. Li, Y. Yu, X. Li, W. Wang, G. Yu, S. Deng, J. Huang, B. Wang, Y. Wang, Maximizing carbon efficiency of petrochemical production from catalytic co-pyrolysis of biomass and plastics using gallium-containing MFI zeolites, Applied Catalysis B: Environmental, 172–173 (2015) 154-164.
- [39] Z. Fang, Z. Hao, Q. Dong, Y. Cui, Bimetallic NiFe 2 O 4 synthesized via confined carburization in NiFe-MOFs for efficient oxygen evolution reaction, Journal of Nanoparticle Research, 20 (2018) 106.
- [40] L. Peng, M. Asgari, P. Mieville, P. Schouwink, S. Bulut, D.T. Sun, Z. Zhou, P. Pattison, W. Van Beek, W.L. Queen, Using Predefined M3 (μ 3-0) Clusters as Building Blocks for an Isostructural Series of Metal–Organic Frameworks, ACS applied materials & interfaces, 9 (2017) 23957-23966.
- [41] P. Horcajada, F. Salles, S. Wuttke, T. Devic, D. Heurtaux, G. Maurin, A. Vimont, M. Daturi, O. David, E. Magnier, How linker's modification controls swelling properties of highly flexible iron (III) dicarboxylates MIL-88, Journal of the American Chemical Society, 133 (2011) 17839-17847.
- [42] K.R. Sanchez-Lievanos, M. Tariq, W.W. Brennessel, K.E. Knowles, Heterometallic trinuclear oxo-centered clusters as single-source precursors for synthesis of stoichiometric monodisperse transition metal ferrite nanocrystals, Dalton Transactions, (2020).
- [43] B. Xu, H. Yang, Y. Cai, H. Yang, C. Li, Preparation and photocatalytic property of spindle-like MIL-88B (Fe) nanoparticles, Inorganic Chemistry Communications, 67 (2016) 29-31.
- [44] M.-H. Pham, G.-T. Vuong, A.-T. Vu, T.-O. Do, Novel route to size-controlled Fe–MIL-88B–NH2 metal–organic framework nanocrystals, Langmuir, 27 (2011) 15261-15267.
- [45] Y.L. Liu, X.J. Zhao, X.X. Yang, Y.F. Li, A nanosized metal-organic framework of Fe-MIL-88NH 2 as a novel peroxidase mimic used for colorimetric detection of glucose, Analyst, 138 (2013) 4526-4531.
- [46] T.-z. Zhang, Y. Lu, Y.-g. Li, Z. Zhang, W.-l. Chen, H. Fu, E.-b. Wang, Metal-organic frameworks constructed from three kinds of new Fe-containing secondary building units, Inorganica Chimica Acta, 384 (2012) 219-224.
- [47] B. Iqbal, M. Saleem, S.N. Arshad, J. Rashid, N. Hussain, M. Zaheer, One-Pot Synthesis of Heterobimetallic Metal–Organic Frameworks (MOFs) for Multifunctional Catalysis, Chemistry–A European Journal, 25 (2019) 10490-10498.
- [48] G.-T. Vuong, M.-H. Pham, T.-O. Do, Synthesis and engineering porosity of a mixed metal Fe 2 Ni MIL-88B metal–organic framework, Dalton Transactions, 42 (2013) 550-557.
- [49] G.-T. Vuong, M.-H. Pham, T.-O. Do, Direct synthesis and mechanism of the formation of mixed metal Fe 2 Ni-MIL-88B, CrystEngComm, 15 (2013) 9694-9703.
- [50] Y. Gu, D. Xie, Y. Wang, W. Qin, H. Zhang, G. Wang, Y. Zhang, H. Zhao, Facile fabrication of composition-tunable Fe/Mg bimetal-organic frameworks for exceptional arsenate removal, Chemical Engineering Journal, 357 (2019) 579-588.

- [51] H. Vrubel, T. Hasegawa, E. de Oliveira, F.S. Nunes, A new facile high yield preparative route for mixed-trinuclear acetate clusters, Inorganic Chemistry Communications, 9 (2006) 208-211.
- [52] A.B. Elmas Kimyonok, M. Ulutürk, Determination of the Thermal Decomposition Products of Terephthalic Acid by Using Curie-Point Pyrolyzer, Journal of Energetic Materials, 34 (2016) 113-122.
- [53] S. Surblé, C. Serre, C. Mellot-Draznieks, F. Millange, G. Férey, A new isoreticular class of metal-organic-frameworks with the MIL-88 topology, Chemical communications, (2006) 284-286.
- [54] K.-Y.A. Lin, H.-A. Chang, C.-J. Hsu, Iron-based metal organic framework, MIL-88A, as a heterogeneous persulfate catalyst for decolorization of Rhodamine B in water, RSC Advances, 5 (2015) 32520-32530.
- [55] J. He, Y. Zhang, X. Zhang, Y. Huang, Highly efficient Fenton and enzyme-mimetic activities of NH 2-MIL-88B (Fe) metal organic framework for methylene blue degradation, Scientific reports, 8 (2018) 1-8.
- [56] K.S. Sing, Reporting physisorption data for gas/solid systems with special reference to the determination of surface area and porosity (Recommendations 1984), Pure and applied chemistry, 57 (1985) 603-619.
- [57] S. Asiri, M. Sertkol, H. Güngüneş, M. Amir, A. Manikandan, İ. Ercan, A. Baykal, The temperature effect on magnetic properties of NiFe 2 O 4 nanoparticles, Journal of Inorganic and Organometallic Polymers and Materials, 28 (2018) 1587-1597.
- [58] P. Samoila, C. Cojocaru, I. Cretescu, C.D. Stan, V. Nica, L. Sacarescu, V. Harabagiu, Nanosized spinel ferrites synthesized by sol-gel autocombustion for optimized removal of azo dye from aqueous solution, Journal of Nanomaterials, 2015 (2015).
- [59] E.R. Kumar, R. Jayaprakash, S. Kumar, Effect of annealing temperature on structural and magnetic properties of manganese substituted NiFe2O4 nanoparticles, Materials science in semiconductor processing, 17 (2014) 173-177.
- [60] D. Sharma, R. Mathur, S. Vadera, N. Kumar, T. Kutty, Synthesis of nanocomposites of Ni–Zn ferrite in aniline formaldehyde copolymer and studies on their pyrolysis products, Journal of alloys and compounds, 358 (2003) 193-204.
- [61] R.Y. Abrokwah, V.G. Deshmane, D. Kuila, Comparative performance of M-MCM-41 (M: Cu, Co, Ni, Pd, Zn and Sn) catalysts for steam reforming of methanol, Journal of Molecular Catalysis A: Chemical, 425 (2016) 10-20.
- [62] Y. Ding, C. Zhao, Y. Li, Z. Ma, X. Lv, Effect of calcination temperature on the structure and catalytic performance of the CU-MCM-41 catalysts for the synthesis of dimethyl carbonate, Química Nova, 41 (2018) 1156-1161.
- [63] G. Elmaci, D. Ozer, B. Zumreoglu-Karan, Liquid phase aerobic oxidation of benzyl alcohol by using manganese ferrite supported-manganese oxide nanocomposite catalyst, Catalysis Communications, 89 (2017) 56-59.
- [64] F. Galvanin, N. Al-Rifai, E. Cao, M. Sankar, G. Hutchings, A. Gavriilidis, V. Dua, Merging information from batch and continuous flow experiments for the identification of kinetic models of benzyl alcohol oxidation over Au-Pd catalyst, in: Computer Aided Chemical Engineering, Elsevier, 2016, pp. 961-966.
- [65] M. Asma, Z. Muhammad, S. Muhammad, V. Wolfgang, Synthesis of lignin model compound containing a β -O-4 linkage, Zeitschrift für Naturforschung B, 72 (2017) 119-124.
- [66] M. Zaheer, R. Kempe, Catalytic hydrogenolysis of aryl ethers: a key step in lignin valorization to valuable chemicals, Acs Catalysis, 5 (2015) 1675-1684.
- [67] A.M. Kulkarni, U.V. Desai, K.S. Pandit, M.A. Kulkarni, P.P. Wadgaonkar, Nickel ferrite nanoparticles–hydrogen peroxide: a green catalyst-oxidant combination in chemoselective oxidation of thiols to disulfides and sulfides to sulfoxides, RSC advances, 4 (2014) 36702-36707.